ORIGINAL PAPER

Global lumped mass formulation for underwater cable dynamics

Xiangqian Zhu · Ali Azmat Sher Khan · Xinyu Li

Abstract The Lumped Mass method is widely utilized for the dynamic modeling of underwater cables. Various element frames, such as the Euler frame, Frenet frame, and Relative Velocity Element Frame (RVEF), have been proposed to express element loads due to their convenience. However, most of these element frames encounter singularity issues when expressing the transformation matrices needed to transfer values between the element frame and the global frame. A Global Lumped Mass Formulation (GLMF) derived from the RVEF is proposed in this paper. The tangential vector and normal plane projection matrix of the element are expressed using global node coordinates. Consequently, the element tension, damping forces, and hydrodynamic forces are also represented in the global frame, effectively eliminating the singularities present in traditional element frames. Moreover, the integration of the Arbitrary Lagrangian–Eulerian (ALE) method with the GLMF is proposed to model cable deployment and retrieval motions. The accuracy of the ALE-GLMF approach is validated against the Arbitrary Lagrangian–Eulerian-Absolute Nodal

Coordinate Formulation. Given that the dynamic response of cables with minimal bending can be calculated efficiently, the GLMF is suitable for modeling towing cables, mooring lines, and ropes with low bending effects.

1 Introduction

Underwater cables play a crucial role in various marine applications, including marine towing systems, floating platforms, and gravity net cage systems [1–5]. Understanding cable dynamics is essential for accurately predicting the responses of marine equipment. The Lumped Mass (LM) method is commonly employed for modeling marine cables [6–10]. Forces acting on the LM element encompass the tension force, damping force, gravity, buoyancy, and hydrodynamic loads. Since tension and damping forces align with the element orientation defined using global node positions, they are easily expressed in the global frame. Similarly, buoyancy and weight act vertically, simplifying their expression in the global frame. However, hydrodynamic loads, which are influenced by relative velocity and acceleration, pose a challenge. Various element frames such as Euler frame, Frenet

X. Zhu (✉) · A. A. S. Khan · X. Li
Key Laboratory of High-Efficiency and Clean Mechanical Manufacture of MOE, National Demonstration Center for Experimental Mechanical Engineering, School of Mechanical Engineering, Shandong University, Jinan 250061, China
e-mail: xqzhu@sdu.edu.cn

frame and RVEF, have been proposed to express hydrodynamic loads decomposed into the tangential and normal directions of the cable. The Euler frame describes element postures using two Euler angles formed by the coordinates of the cable nodes [11–13]. Although the Euler frame is conceptually straightforward, it encounters singularity issues in certain postures due to inverse trigonometric functions. On the other hand, the Frenet frame employs orthogonal basis vectors—tangential, normal, and binormal vectors—generated based on the shape function of the entire cable [14, 15]. The normal vector is derived from the tangential vector, while the binormal vector is determined by the cross product of the tangential and normal vectors. However, the Frenet frame encounters singularity when adjacent cable elements align to form a straight line. In contrast, the RVEF addresses this limitation by establishing a plane using the tangential vector and the relative velocity of the element. Subsequently, the RVEF is generated based on the tangential vector and normal vector of the plane. The RVEF employs the global relative velocity to express hydrodynamic loads, dividing them into tangential and non-tangential components. Despite this advancement, the element frame remains necessary to define the direction of hydrodynamic loads, leading to mathematical singularities when the tangential vector aligns with the relative velocity [1, 16]. Consequently, these frames exhibit singularities in specific configurations, complicating the resolution of dynamic equations.

In this study, a Global Lumped Mass Formulation (GLMF) is proposed to directly express hydrodynamic loads with respect to the tangential vector and normal plane, generated using global node coordinates. The global relative velocity is projected into tangential and non-tangential components for the calculation of hydrodynamic loads. By expressing all loads directly in the global frame, the GLMF eliminates the need for the coordinate transformation operations, resulting in two key advantages: increased efficiency and the absence of singularities. The hydrodynamic loads in the RVEF are closely related to those in the GLMF, and the derivation from the RVEF to the GLMF is detailed in Sect. 2. Additionally, a case study involving a constant-length cable driven by a screw route is simulated, demonstrating that the GLMF is more efficient than the RVEF while maintaining nearly the same level of accuracy.

In some marine equipment, the cable length changes via winches, as seen in deep-sea towing systems [3], deep-sea pipeline installations [17]. To precisely analyze the dynamic response of these systems, the deployment and retrieval motions must be considered in the cable model. Some studies use a combination of Lagrangian–Eulerian description and Absolute Nodal Coordinate Formulation (ALE-ANCF) to model flexible cables with variable length [17, 18]. While ALE-ANCF performs well in modeling flexible cables with large bending deformations, its drawback lies in the introduction of spatial gradients by ANCF. Consequently, the number of coordinates in ALE-ANCF is at least seven times the number of nodes (three position coordinates, three spatial gradients, one physical coordinate). In this study, the Lagrangian–Eulerian description is incorporated into the GLMF to model cables with variable length. Each node in ALE-GLMF has only four coordinates (three position coordinates, one physical coordinate). To verify the performance of ALE-GLMF, cables driven by circular, straight-line, and screw routes with increasing length are modeled using both ALE-GLMF and ALE-ANCF. Additionally, a contact model between the cable nodes and the seabed is incorporated into both ALE-GLMF and ALE-ANCF to simulate the cable laying process with identical cable nodes. Although unsmooth broken lines are generated in ALE-GLMF when the cable elements encounter the seabed, the positions of the cable sections laying on the seabed are nearly identical in both ALE-GLMF and ALE-ANCF. Given that the element lengths in both methods are identical in this case, ALE-GLMF proves to be more efficient than ALE-ANCF. Therefore, compared to ANCF or ALE-ANCF, GLMF and ALE-GLMF offer a better choice for modeling cables with low bending deformation, especially in situations where a higher number of cable nodes is required to represent concentrated loads or mass points.

This paper is organized as follows: Sect. 2 introduces the numerical models and singularities of the Lumped Mass (LM) method with Euler frame, Frenet frame, RVEF, and GLMF. Section 3 presents the numerical model of ALE-GLMF for cables with variable length, including comparisons between the ALE-GLMF and ALE-ANCF in various scenarios. Finally, the conclusions are provided in Sect. 4.
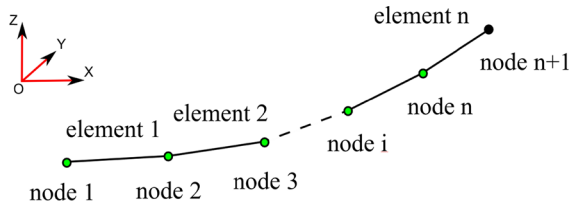
Fig. 1 Spatial discretization of LM

2 LM method

The LM method divides the flexible cable into many elements, as shown in Fig. 1. The element forces, including hydrodynamic loads, tension, damping force, gravity and buoyancy are distributed into the element terminal nodes [19–21]. The element forces are divided into external and internal forces as shown in Eqs. (1) and (2). The mass matrix, gravity in water, drag resistance force, and added mass effect acting on the node i are represented using $\mathbf{M}_{node\,i}^g$, $\mathbf{G}_{node\,i}^g$, $\mathbf{F}_{node\,i}^{dg}$, and $\mathbf{F}_{node\,i}^{ag}$, respectively. $\mathbf{M}_{ele\,j}^g$, $\mathbf{G}_{ele\,j}^g$, $\mathbf{F}_{ele\,j}^{dg}$, and $\mathbf{F}_{ele\,j}^{ag}$ are the mass matrix, gravity in water, drag resistance force, and added mass effect acting on the element i, respectively. $\mathbf{T}_{node\,i}^g$ and $\mathbf{D}_{node\,i}^g$ of Eq. (2) indicate the stiffness and damping forces acting on the node i, respectively. While, $\mathbf{T}_{ele\,i}^g$ and $\mathbf{D}_{ele\,i}^g$ are the stiffness and damping forces acting on the element i, respectively.

$$
\begin{cases}
\mathbf{M}_{node\,i}^g = \dfrac{1}{2}\left(\mathbf{M}_{ele\,i-1}^g + \mathbf{M}_{ele\,i}^g\right) \\
\mathbf{G}_{node\,i}^g = \dfrac{1}{2}\left(\mathbf{G}_{ele\,i-1}^g + \mathbf{G}_{ele\,i}^g\right) \\
\mathbf{F}_{node\,i}^{dg} = \dfrac{1}{2}\left(\mathbf{F}_{ele\,i-1}^{dg} + \mathbf{F}_{ele\,i}^{dg}\right) \\
\mathbf{F}_{node\,i}^{ag} = \dfrac{1}{2}\left(\mathbf{F}_{ele\,i-1}^{ag} + \mathbf{F}_{ele\,i}^{ag}\right)
\end{cases}
(i = 2, 3, .., n-1)
\tag{1}
$$

$$
\begin{cases}
\mathbf{T}_{node\,i}^g = -\mathbf{T}_{ele\,i-1}^g + \mathbf{T}_{ele\,i}^g \\
\mathbf{D}_{node\,i}^g = -\mathbf{D}_{ele\,i-1}^g + \mathbf{D}_{ele\,i}^g
\end{cases}
(i = 2, 3, .., n-1)
\tag{2}
$$

The mass matrix $\mathbf{M}$, force sum $\mathbf{F}$ and the acceleration vectors $\ddot{\mathbf{q}}$ of cable are shown in Eqs. (3–5).

$$
\mathbf{M} = \begin{bmatrix}
\mathbf{M}_{node1}^g & \mathbf{0} & ... & \mathbf{0} \\
\mathbf{0} & \mathbf{M}_{node2}^g & ... & \mathbf{0} \\
... & ... & ... & ... \\
\mathbf{0} & \mathbf{0} & ... & \mathbf{M}_{node\,n}^g
\end{bmatrix}
\tag{3}
$$

$$
\mathbf{F} = \begin{bmatrix}
\mathbf{G}_{node1}^g + \mathbf{T}_{node1}^g + \mathbf{D}_{node1}^g + \mathbf{F}_{node1}^{dg} + \mathbf{F}_{node1}^{ag} \\
\mathbf{G}_{node2}^g + \mathbf{T}_{node2}^g + \mathbf{D}_{node2}^g + \mathbf{F}_{node2}^{dg} + \mathbf{F}_{node2}^{ag} \\
... \\
\mathbf{G}_{node\,n}^g + \mathbf{T}_{node\,n}^g + \mathbf{D}_{node\,n}^g + \mathbf{F}_{node\,n}^{dg} + \mathbf{F}_{node\,n}^{ag}
\end{bmatrix}
\tag{4}
$$

$$
\ddot{\mathbf{q}} = \begin{bmatrix} \ddot{\mathbf{q}}_{node\,1}^T & \ddot{\mathbf{q}}_{node2}^T & ... & \ddot{\mathbf{q}}_{node\,n}^T \end{bmatrix}^T
\tag{5}
$$

where $\ddot{\mathbf{q}}_{node\,i}$ is the acceleration vector of node i.

The equation of motion of the cable is established using Baumgarten's stabilization method [22] as Eq. (6).

$$
\begin{cases}
\boldsymbol{\gamma} = -\left(\boldsymbol{\Phi}_q \dot{\mathbf{q}}\right)_q \dot{\mathbf{q}} - 2\boldsymbol{\Phi}_{qt}\dot{\mathbf{q}} - \boldsymbol{\Phi}_{tt} \\
\begin{bmatrix} \mathbf{M} & \boldsymbol{\Phi}_{\mathbf{q}}^T \\ \boldsymbol{\Phi}_{\mathbf{q}} & \mathbf{0} \end{bmatrix}\begin{bmatrix} \ddot{\mathbf{q}} \\ \boldsymbol{\lambda} \end{bmatrix} = \begin{bmatrix} \mathbf{F} \\ \boldsymbol{\gamma} - \alpha\boldsymbol{\Phi} - \beta\dfrac{d\boldsymbol{\Phi}}{dt} \end{bmatrix}
\end{cases}
\tag{6}
$$

where $\boldsymbol{\Phi}$ is constraint vector. $\boldsymbol{\Phi}_q$ is Jacobian matrix of $\boldsymbol{\Phi}$ with respect to $\mathbf{q}$. $\boldsymbol{\lambda}$ is the Lagrangian multiplier.

The differences among the Euler frame, Frenet frame, RVEF, and GLMF lie in how they express the element mass and forces. The Euler frame uses Euler angles to define the element frame, while the Frenet frame defines the element frame based on the cable shape function. The RVEF defines the element frame by the relative velocity of the cable element compared to the seawater. In contrast, the GLMF does not use any element frame, its mass matrices and forces are all expressed directly in the global frame. After mathematical derivation, it is shown that the RVEF and GLMF are essentially equivalent, resulting in almost the same accuracy for both methods. However, the GLMF offers greater computational robustness compared to the RVEF. This section introduces the details of the Euler frame, Frenet frame, RVEF, and GLMF, as well as the derivation from the RVEF to the GLMF.

2.1 Euler frame

The rotation angles of the Z-Y-X sequence are 0, $\theta_{ele\,i}$ and $\varphi_{ele\,i}$ as shown in Fig. 2, respectively.

The transformation matrix from the element frame to the global frame is written as Eq. (7) [23, 24].

$$
\mathbf{A}_{ele\,i}^{trans} = \begin{bmatrix}
\cos\theta_{ele\,i} & \sin\theta_{ele\,i}\sin\varphi_{ele\,i} & \sin\theta_{ele\,i}\cos\varphi_{ele\,i} \\
0 & \cos\varphi_{ele\,i} & -\sin\varphi_{ele\,i} \\
-\sin\theta_{ele\,i} & \cos\theta_{ele\,i}\sin\varphi_{ele\,i} & \cos\theta_{ele\,i}\cos\varphi_{ele\,i}
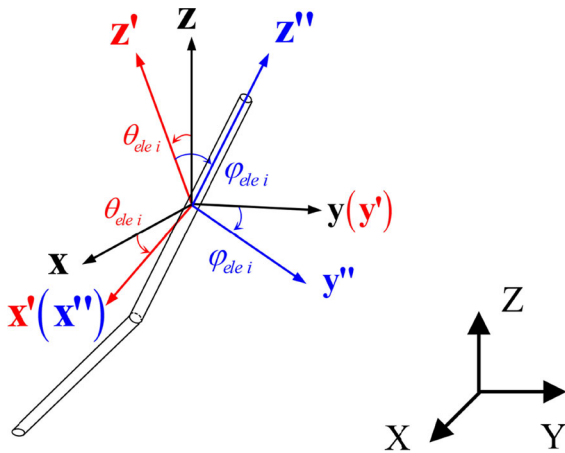\end{bmatrix}
\tag{7}
$$

Fig. 2 Euler angles in element frame

The $\theta_{ele\,i}$ and $\varphi_{ele\,i}$ can be expressed by the position vectors of node i and node $i + 1$ in global frame, as shown in Eqs. (8–9) [25].

$$\theta_{ele\,i} = \tan^{-1}\left(\frac{r^x_{node\,i+1} - r^x_{node\,i}}{r^z_{node\,i+1} - r^z_{node\,i}}\right) \qquad (8)$$

$$\phi_{ele\,i} = \begin{cases} \tan^{-1}\dfrac{\left(r^y_{node\,i} - r^y_{node\,i+1}\right)\cos\theta_{ele\,i}}{r^z_{node\,i+1} - r^z_{node\,i}} & (\cos\theta_{ele\,i} > \sin\theta_{ele\,i}) \\[2ex] \tan^{-1}\dfrac{\left(r^y_{node\,i} - r^y_{node\,i+1}\right)\sin\theta_{ele\,i}}{r^x_{node\,i+1} - r^x_{node\,i}} & (\cos\theta_{ele\,i} \le \sin\theta_{ele\,i}) \end{cases} \qquad (9)$$

where $r^x_{node\,i}$, $r^y_{node\,i}$ and $r^z_{node\,i}$ are the x-, y- and z-coordinate of the node i in global frame, respectively.

The mass matrix and forces acting on the element i are sorted as external forces and internal forces. The internal forces are composed of the tension and damping force. The tension is related to the axial strain, and the damping force is related to the change ratio of the axial strain as Eq. (10).

$$\begin{cases} \mathbf{E}^g_{ele\,i} = \mathbf{r}_{node\,i+1} - \mathbf{r}_{node\,i} \\[1ex] l_{ele\,i} = \sqrt{\left(\mathbf{E}^g_{ele\,i}\right)^T \mathbf{E}^g_{ele\,i}} \\[1ex] \mathbf{z}^g_{ele\,i} = \begin{bmatrix} \mathbf{A}^{trans}_{ele\,i}(3,1) & \mathbf{A}^{trans}_{ele\,i}(3,2) & \mathbf{A}^{trans}_{ele\,i}(3,3) \end{bmatrix}^T \\[1ex] \varepsilon_{ele\,i} = \left[\sqrt{\left(\mathbf{E}^g_{ele\,i}\right)^T \mathbf{E}^g_{ele\,i}}\Big/ l^0_{ele\,i}\right] - 1 \\[1ex] \mathbf{T}^g_{ele\,i} = \dfrac{\pi d^2_c}{4} E\varepsilon_{ele\,i}\mathbf{z}^g_{ele\,i} \\[1ex] \mathbf{D}^g_{ele\,i} = \dfrac{cE\pi d^2_c}{4}\left(\mathbf{z}^g_{ele\,i}\right)^T(\dot{\mathbf{r}}_{node\,i+1} - \dot{\mathbf{r}}_{node\,i})\mathbf{z}^g_{ele\,i} \end{cases} \qquad (10)$$

The element external forces expressed in global frame are composed of the gravity, drag resistance force and added mass effect as shown in Eq. (11) [26–28].

$$\begin{cases} \mathbf{v}^l_{ele\,i} = \left(\mathbf{A}^{trans}_{ele\,i}\right)^T\left[\mathbf{v}_w - \dfrac{1}{2}(\dot{\mathbf{r}}_{node\,i+1} + \dot{\mathbf{r}}_{node\,i})\right] \\[2ex] \mathbf{F}^{dg}_{ele\,i} = \mathbf{A}^{trans}_{ele\,i}\begin{bmatrix} \dfrac{1}{2}C_n\rho_f d_c l_{ele\,i}\left|v^{lx}_{ele\,i}\right|v^{lx}_{ele\,i} \\[1.5ex] \dfrac{1}{2}C_n\rho_f d_c l_{ele\,i}\left|v^{ly}_{ele\,i}\right|v^{ly}_{ele\,i} \\[1.5ex] \dfrac{\pi}{2}C_f\rho_f d_c l_{ele\,i}\left|v^{lz}_{ele\,i}\right|v^{lz}_{ele\,i} \end{bmatrix} \\[5ex] \mathbf{F}^{ag}_{ele\,i} = \dfrac{\pi}{4}(1+C_m)l^0_{ele\,i}d^2\rho_f\mathbf{A}^{trans}_{ele\,i}\begin{bmatrix} 1 & 0 & 0 \\ 0 & 1 & 0 \\ 0 & 0 & 0 \end{bmatrix}\mathbf{A}^T_{trans}\mathbf{a}_w \\[4ex] \mathbf{G}^g_{ele\,i} = \begin{bmatrix} 0 & 0 & -\dfrac{\pi d^2_c}{4}l^0_{ele\,i}\rho_c g \end{bmatrix}^T \\[2ex] \mathbf{B}^g_{ele\,i} = \begin{bmatrix} 0 & 0 & \dfrac{\pi d^2_c}{4}l^0_{ele\,i}\rho_f g \end{bmatrix}^T \end{cases} \qquad (11)$$

$$\mathbf{M}^g_{ele\,i} = \left(\mathbf{A}^{trans}_{ele\,i}\right)^T$$
$$\begin{bmatrix} \dfrac{\pi d^2_c}{4}l^0_{ele\,i}(\rho_c + C_m\rho_f) & 0 & 0 \\[2ex] 0 & \dfrac{\pi d^2_c}{4}l^0_{ele\,i}(\rho_c + C_m\rho_f) & 0 \\[2ex] 0 & 0 & \dfrac{\pi d^2_c}{4}l^0_{ele\,i}\rho_c \end{bmatrix}\mathbf{A}^{trans}_{ele\,i} \qquad (12)$$

where $\mathbf{v}^l_{ele\,i}$ is the relative velocity between the seawater and element i in element frame, and $v^{lx}_{ele\,i}$, $v^{ly}_{ele\,i}$ and $v^{lz}_{ele\,i}$ are the x-, y- and z-component of $\mathbf{v}^l_{ele\,i}$, respectively. $\mathbf{v}_w$ is the seawater velocity in global frame. $\mathbf{F}^{dg}_{ele\,i}$, $\mathbf{F}^{ag}_{ele\,i}$, $\mathbf{G}^g_{ele\,i}$ and $\mathbf{B}^g_{ele\,i}$ are the drag resistance force, added mass effects, gravity and buoyancy acting on the element i in global frame, respectively. $|\cdot|$ denotes the absolute value of $\cdot$. C_f and C_n are the tangential and normal drag resistance coefficients, respectively. C_m is the added mass coefficient. ρ_c and ρ_f are the densities of cable and seawater, respectively. $\mathbf{a}_w$ is the acceleration of seawater, and g is the gravity acceleration.

The mass matrix of element i with respect to the global frame is written as Eq. (12) [29].
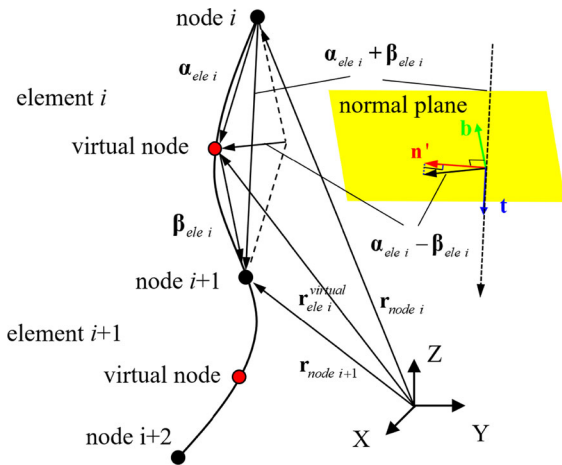
Fig. 3 Frenet frame generated using virtual node

2.2 Frenet frame

The shape function of the cable is used to define the element frame in the Frenet frame, as shown in Fig. 3. Further details can be found in references [30, 31].

All the node positions are used to form three spline functions from the top node to the last node in the global frame. Three functions are named as f_X, f_Y and f_Z, and the global coordinates of the P point can be calculated by Eq. (13).

$$\begin{cases} X_p = f_X\left(l_p^0\right) \\ Y_p = f_Y\left(l_p^0\right) \\ Z_p = f_Z\left(l_p^0\right) \end{cases} \tag{13}$$

where X_p, Y_p and Z_p are the global coordinates of the P point. l_p^0 is the span length of the P point.

A virtual node positioned in the middle of each element can be obtained by using Eq. (13), and vectors $\boldsymbol{\alpha}_{ele\,i}$ and $\boldsymbol{\beta}_{ele\,i}$ defined by the element terminal nodes and the virtual node are defined in Eq. (14).

$$\begin{cases} \boldsymbol{\alpha}_{ele\,i} = \mathbf{r}_{ele\,i}^{virtual} - \mathbf{r}_{node\,i} \\ \boldsymbol{\beta}_{ele\,i} = \mathbf{r}_{node\,i+1} - \mathbf{r}_{ele\,i}^{virtual} \end{cases} \tag{14}$$

Finally, the tangential, normal and binormal unit vectors $\mathbf{t}_{ele\,i}$, $\mathbf{n}_{ele\,i}$ and $\mathbf{b}_{ele\,i}$ are defined in Eq. (15), respectively.

$$\begin{cases} \mathbf{t}_{ele\,i} = \dfrac{\boldsymbol{\alpha}_{ele\,i} + \boldsymbol{\beta}_{ele\,i}}{\|\boldsymbol{\alpha}_{ele\,i} + \boldsymbol{\beta}_{ele\,i}\|} \\ \mathbf{n}'_{ele\,i} = (\boldsymbol{\alpha}_{ele\,i} - \boldsymbol{\beta}_{ele\,i})\left(\mathbf{I}_{3\times3} - \mathbf{t}_{ele\,i}\mathbf{t}_{ele\,i}^{\mathbf{T}}\right) \\ \mathbf{n}_{ele\,i} = \dfrac{\mathbf{n}'_{ele\,i}}{\|\mathbf{n}'_{ele\,i}\|} \\ \mathbf{b}_{ele\,i} = \mathbf{t}_{ele\,i} \times \mathbf{n}_{ele\,i} \end{cases} \tag{15}$$

where $\mathbf{n}'_{ele\,i}$ is projection of the $(\boldsymbol{\alpha}_{ele\,i} - \boldsymbol{\beta}_{ele\,i})$ in the normal plane. $\mathbf{I}_{3\times3}$ is a three-order unit matrix.

The transformation matrix $\mathbf{A}_{ele\,i}^{trans}$ is written as,

$$\mathbf{A}_{ele\,i}^{trans} = \begin{bmatrix} \mathbf{t}_{ele\,i} & \mathbf{n}_{ele\,i} & \mathbf{b}_{ele\,i} \end{bmatrix} \tag{16}$$

2.3 RVEF

The element frame is defined by using the tangential vector and relative velocity in the RVEF, and three unit vectors are shown in Eq. (17) and Fig. 4.

$$\begin{cases} \mathbf{v}_{ele\,i}^g = \mathbf{v}_w - \dfrac{1}{2}(\dot{\mathbf{r}}_{node\,i+1} + \dot{\mathbf{r}}_{node\,i}) \\ \mathbf{z}_{ele\,i}^g = \dfrac{\mathbf{E}_{ele\,i}^g}{\|\mathbf{E}_{ele\,i}^g\|} \\ \mathbf{x}_{ele\,i}^g = \dfrac{\mathbf{z}_{ele\,i}^g \times \mathbf{v}_{ele\,i}^g}{\|\mathbf{z}_{ele\,i}^g \times \mathbf{v}_{ele\,i}^g\|} \\ \mathbf{y}_{ele\,i}^g = \mathbf{z}_{ele\,i}^g \times \mathbf{x}_{ele\,i}^g \end{cases} \tag{17}$$

The transformation matrix $\mathbf{A}_{ele\,i}^{trans}$ is defined as,

$$\mathbf{A}_{ele\,i}^{trans} = \begin{bmatrix} \mathbf{x}_{ele\,i}^g & \mathbf{y}_{ele\,i}^g & \mathbf{z}_{ele\,i}^g \end{bmatrix} \tag{18}$$

Because the relative velocity is merely decomposed in two directions, the drag resistance force of element i with respect to the global frame is written as,

$$\mathbf{F}_{ele\,i}^{dg} = \mathbf{A}_{ele\,i}^{trans} \begin{bmatrix} 0 \\ -\dfrac{1}{2}C_n\rho_f d_c l_{ele\,i} \left\|\mathbf{z}_{ele\,i}^g \times \mathbf{v}_{ele\,i}^g\right\|^2 \\ \dfrac{\pi}{2}C_f\rho_f d_c l_{ele\,i} (\mathbf{z}_{ele\,i}^g)^T \mathbf{v}_{ele\,i}^g \left|(\mathbf{z}_{ele\,i}^g)^T \mathbf{v}_{ele\,i}^g\right| \end{bmatrix} \tag{19}$$

$$\begin{cases} \mathbf{z}_{ele\,i}^{g} = \dfrac{\mathbf{E}_{ele\,i}^{g}}{\|\mathbf{E}_{ele\,i}^{g}\|} \\[6pt] \mathbf{P}_{ele\,i} = \mathbf{I}_{3\times3} - \mathbf{z}_{ele\,i}^{g}(\mathbf{z}_{ele\,i}^{g})^{T} \\[6pt] \mathbf{F}_{ele\,i}^{dg} = \dfrac{1}{2} C_{n}\rho_{f} d_{c} l_{ele\,i}\|\mathbf{P}_{ele\,i}\mathbf{v}_{ele\,i}^{g}\|\mathbf{P}_{ele\,i}\mathbf{v}_{ele\,i}^{g} + \dfrac{\pi}{2} C_{f}\rho_{f} d_{c} l_{ele\,i}\left|(\mathbf{z}_{ele\,i}^{g})^{T}\mathbf{v}_{ele\,i}^{g}\right|\mathbf{z}_{ele\,i}^{g}(\mathbf{z}_{ele\,i}^{g})^{T}\mathbf{v}_{ele\,i}^{g} \\[6pt] \mathbf{F}_{ele\,i}^{ag} = \dfrac{\pi}{4}(1+C_{m})d^{2}\rho_{f} l_{ele\,i}^{0}\mathbf{P}_{ele\,i}\mathbf{a}_{w} \\[6pt] \mathbf{M}_{ele\,i}^{g} = \dfrac{\pi d_{c}^{2}}{4} l_{ele\,i}^{0}\rho_{c}\mathbf{I}_{3\times3} + C_{A}\dfrac{\pi d_{c}^{2}}{4} l_{ele\,i}^{0}\rho_{f}\mathbf{P}_{ele\,i} \end{cases} \tag{20}$$

The mass matrix and the other forces including $\mathbf{M}_{ele\,i}^{g}$, $\mathbf{F}_{ele\,i}^{ag}$, $\mathbf{G}_{ele\,i}^{g}$ and $\mathbf{B}_{ele\,i}^{g}$ are same as Eq. (1) and Eq. (11).

2.4 GLMF

The element forces and mass matrices in GLMF are all expressed using node positions in global frame. The relative velocity $\mathbf{v}_{ele\,i}^{g}$ is decomposed into tangential and normal velocity, and the normal velocity is obtained by a projection matrix $\mathbf{P}_{ele\,i}$, as shown in Fig. 5. The drag resistance force and added mass matrices are expressed as Eq. (20).

2.5 Derivation GLMF from RVEF

The global relative velocity is decomposed into tangential and non-tangential two components in the RVEF, and the global relative velocity is directly used to express the hydrodynamic loads, as shown in
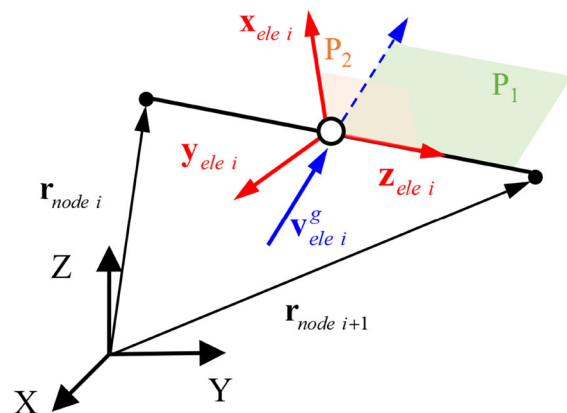
Eq. (19), but the element frame is still needed to direct the load directions.

Because the tangential component of the global relative velocity is easy to define using the global node coordinates, the hydrodynamic loads can be expressed in global frame if the normal component can be defined using the global node coordinates together with the global velocity vectors. The Eq. (21) is proved here.

$$\mathbf{P}_{ele\,i}\mathbf{v}_{ele\,i}^{g} = -\|\mathbf{z}_{ele\,i}^{g}\times\mathbf{v}_{ele\,i}^{g}\|\mathbf{y}_{ele\,i} \tag{21}$$

Firstly, the $\mathbf{P}_{ele\,i}\mathbf{v}_{ele\,i}^{g}$ is proved to be parallel with the $-\|\mathbf{z}_{ele\,i}^{g}\times\mathbf{v}_{ele\,i}^{g}\|\mathbf{y}_{ele\,i}$. $-\|\mathbf{z}_{ele\,i}^{g}\times\mathbf{v}_{ele\,i}^{g}\|\mathbf{y}_{ele\,i}$ is in the direction of $\mathbf{y}_{ele\,i}$ which is orthogonal with the $\mathbf{x}_{ele\,i}$ and $\mathbf{z}_{ele\,i}$. Therefore, $\mathbf{P}_{ele\,i}\mathbf{v}_{ele\,i}^{g}$ and $-\|\mathbf{z}_{ele\,i}^{g}\times\mathbf{v}_{ele\,i}^{g}\|\mathbf{y}_{ele\,i}$ are parallel if $\mathbf{P}_{ele\,i}\mathbf{v}_{ele\,i}^{g}$ is vertical to both the $\mathbf{x}_{ele\,i}$ and $\mathbf{z}_{ele\,i}$ [32, 33]. The $\mathbf{P}_{ele\,i}\mathbf{v}_{ele\,i}^{g}$ is proved to be vertical to both the $\mathbf{x}_{ele\,i}$ and $\mathbf{z}_{ele\,i}$ in Eqs. (22–23).

$$\begin{aligned} (\mathbf{x}_{ele\,i}^{g})^{T}\mathbf{P}_{ele\,i}\mathbf{v}_{ele\,i}^{g} &= (\mathbf{x}_{ele\,i}^{g})^{T}\left[\mathbf{I}_{3\times3} - \mathbf{z}_{ele\,i}^{g}(\mathbf{z}_{ele\,i}^{g})^{T}\right]\mathbf{v}_{ele\,i}^{g} \\ &= (\mathbf{x}_{ele\,i}^{g})^{T}\left[\mathbf{v}_{ele\,i}^{g} - \mathbf{z}_{ele\,i}^{g}(\mathbf{z}_{ele\,i}^{g})^{T}\mathbf{v}_{ele\,i}^{g}\right] \\ &= (\mathbf{x}_{ele\,i}^{g})^{T}\mathbf{v}_{ele\,i}^{g} - (\mathbf{x}_{ele\,i}^{g})^{T}\mathbf{z}_{ele\,i}^{g}(\mathbf{z}_{ele\,i}^{g})^{T}\mathbf{v}_{ele\,i}^{g} = \mathbf{0} \end{aligned} \tag{22}$$

$$\begin{aligned} (\mathbf{z}_{ele\,i}^{g})^{T}\mathbf{P}_{ele\,i}\mathbf{v}_{ele\,i}^{g} &= (\mathbf{z}_{ele\,i}^{g})^{T}\left[\mathbf{I}_{3\times3} - \mathbf{z}_{ele\,i}^{g}(\mathbf{z}_{ele\,i}^{g})^{T}\right]\mathbf{v}_{ele\,i}^{g} \\ &= (\mathbf{z}_{ele\,i}^{g})^{T}\left[\mathbf{v}_{ele\,i}^{g} - \mathbf{z}_{ele\,i}^{g}(\mathbf{z}_{ele\,i}^{g})^{T}\mathbf{v}_{ele\,i}^{g}\right] \\ &= (\mathbf{z}_{ele\,i}^{g})^{T}\mathbf{v}_{ele\,i}^{g} - (\mathbf{z}_{ele\,i}^{g})^{T}\mathbf{z}_{ele\,i}^{g}(\mathbf{z}_{ele\,i}^{g})^{T}\mathbf{v}_{ele\,i}^{g} = \mathbf{0} \end{aligned} \tag{23}$$

Therefore, $\mathbf{P}_{ele\,i}\mathbf{v}_{ele\,i}^{g}$ can be expressed by using $-\|\mathbf{z}_{ele\,i}\times\mathbf{v}_{ele\,i}^{g}\|\mathbf{y}_{ele\,i}$, as shown in Eq. (24).

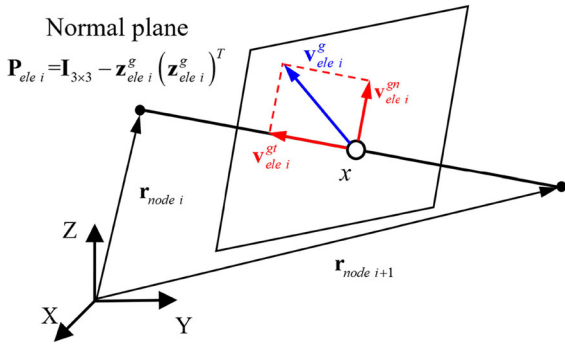$$\mathbf{P}_{ele\,i}\mathbf{v}_{ele\,i}^{g} = -k\|\mathbf{z}_{ele\,i}\times\mathbf{v}_{ele\,i}^{g}\|\mathbf{y}_{ele\,i} \tag{24}$$

Fig. 4 RVEF generated using relative velocity

Fig. 5 Decomposing relative velocity in GLMF

A proposition that $k = 1$ is proved here. Left multiply $\left(-\left\|\mathbf{z}_{ele\,i}^{g} \times \mathbf{v}_{ele\,i}^{g}\right\|\mathbf{y}_{ele\,i}^{g}\right)^{T}$ on both sides of Eq. (24).

$$\left(-\left\|\mathbf{z}_{ele\,i}^{g} \times \mathbf{v}_{ele\,i}^{g}\right\|\mathbf{y}_{ele\,i}^{g}\right)^{T}\mathbf{P}_{ele\,i}\mathbf{v}_{ele\,i}^{g} = k\left(\left\|\mathbf{z}_{ele\,i}^{g} \times \mathbf{v}_{ele\,i}^{g}\right\|\mathbf{y}_{ele\,i}^{g}\right)^{T}\left\|\mathbf{z}_{ele\,i} \times \mathbf{v}_{ele\,i}^{g}\right\|\mathbf{y}_{ele\,i} \tag{25}$$

Combing Eqs. (20) and (25), the result can be written as,

$$-\left\|\mathbf{z}_{ele\,i} \times \mathbf{v}_{ele\,i}^{g}\right\|\left(\mathbf{v}_{ele\,i}^{g}\right)^{T}\mathbf{y}_{ele\,i}^{g} = k\left\|\mathbf{z}_{ele\,i}^{g} \times \mathbf{v}_{ele\,i}^{g}\right\|^{2} \tag{26}$$

Combining Eqs. (17) and (26), the result can be written as,

$$-\left(\mathbf{v}_{ele\,i}^{g}\right)^{T}\tilde{\mathbf{z}}_{ele\,i}^{g}\tilde{\mathbf{z}}_{ele\,i}^{g}\mathbf{v}_{ele\,i}^{g} = k\left\|\mathbf{z}_{ele\,i}^{g} \times \mathbf{v}_{ele\,i}^{g}\right\|^{2} \tag{27}$$

The skew symmetric matrices can be written as Eq. (28).

$$\left(\mathbf{z}_{ele\,i}^{g} \times \mathbf{v}_{ele\,i}^{g}\right)^{T}\left(\mathbf{z}_{ele\,i}^{g} \times \mathbf{v}_{ele\,i}^{g}\right) = k\left\|\mathbf{z}_{ele\,i}^{g} \times \mathbf{v}_{ele\,i}^{g}\right\|^{2} \tag{28}$$

Finally, $k = 1$ is derived from Eq. (28), and the Eq. (21) has been proved.

Combining Eqs. (19) and (21), the drag force derivation from the RVEF to the GLMF can be written as Eq. (29).

$$\mathbf{F}_{ele\,i}^{dg} = \mathbf{A}_{ele\,i}^{trans}\begin{bmatrix} 0 \\ -\frac{1}{2}C_{n}\rho_{f}d_{c}l_{ele\,i}\left\|\mathbf{z}_{ele\,i}^{g} \times \mathbf{v}_{ele\,i}^{g}\right\|^{2} \\ \frac{\pi}{2}C_{f}\rho_{f}d_{c}l_{ele\,i}\left(\mathbf{z}_{ele\,i}^{g}\right)^{T}\mathbf{v}_{ele\,i}^{g}\left|\left(\mathbf{z}_{ele\,i}^{g}\right)^{T}\mathbf{v}_{ele\,i}^{g}\right| \end{bmatrix}$$
$$= \frac{1}{2}C_{n}\rho_{f}d_{c}l_{ele\,i}\left\|\mathbf{P}_{ele\,i}\mathbf{v}_{ele\,i}^{g}\right\|\mathbf{P}_{ele\,i}\mathbf{v}_{ele\,i}^{g}$$
$$+ \frac{\pi}{2}C_{f}\rho_{f}d_{c}l_{ele\,i}\left|\left(\mathbf{z}_{ele\,i}^{g}\right)^{T}\mathbf{v}_{ele\,i}^{g}\right|\mathbf{z}_{ele\,i}^{g}\left(\mathbf{z}_{ele\,i}^{g}\right)^{T}\mathbf{v}_{ele\,i}^{g} \tag{29}$$

Combining with Eqs. (21) and (11), the added mass effect derivation from the RVEF to the GLMF can also be written as Eq. (30).

$$\mathbf{F}_{ele\,i}^{ag} = \frac{\pi}{4}(1 + C_{m})d^{2}\rho_{f}l_{ele\,i}^{0}\mathbf{P}_{ele\,i}\mathbf{a}_{w} \tag{30}$$

The derivation of $\mathbf{M}_{ele\,i}^{g}$ from the RVEF to the GLMF is written as Eq. (31). Finally, the derivation process from the RVEF to the GLMF is completed.

$$\mathbf{M}_{ele\,i}^{g} = \left(\mathbf{A}_{ele\,i}^{trans}\right)^{T}\begin{bmatrix} \frac{\pi d_{c}^{2}}{4}l_{ele\,i}^{0}(\rho_{c} + C_{m}\rho_{f}) & 0 & 0 \\ 0 & \frac{\pi d_{c}^{2}}{4}l_{ele\,i}^{0}(\rho_{c} + C_{m}\rho_{f}) & 0 \\ 0 & 0 & \frac{\pi d_{c}^{2}}{4}l_{ele\,i}^{0}\rho_{c} \end{bmatrix}\mathbf{A}_{ele\,i}^{trans}$$
$$= \left(\mathbf{A}_{ele\,i}^{trans}\right)^{T}\left(\frac{\pi d_{c}^{2}}{4}l_{ele\,i}^{0}\rho_{c}\mathbf{I}_{3\times3} + C_{m}\frac{\pi d_{c}^{2}}{4}l_{ele\,i}^{0}\rho_{f}\begin{bmatrix} 1 & 0 & 0 \\ 0 & 1 & 0 \\ 0 & 0 & 0 \end{bmatrix}\right)\mathbf{A}_{ele\,i}^{trans}$$
$$= \frac{\pi d_{c}^{2}}{4}l_{ele\,i}^{0}\rho_{c}\mathbf{I}_{3\times3} + C_{m}\frac{\pi d_{c}^{2}}{4}l_{ele\,i}^{0}\rho_{f}\mathbf{P}_{ele\,i} \tag{31}$$

To verify the accuracy of the GLMF, a constant-length cable driven along a screw route is simulated by using the GLMF, RVEF and Euler Frame, respectively. This scenario is referred to as Case 1. As shown in Fig. 6, the initial position of the cable is a straight line, which is a singularity case for the Frenet frame. The trace of the top node is illustrated in Fig. 7. The diameter of the screw route is 40 m, with the top node traveling 62.8 m along the Z-axis for every circular motion completed in 62.8 s. The screw route is depicted for the first 100 s but continues for 2000s in total. The X-, Y- and Z-coordinate of the last node over time are shown in Figs. 8, 9, 10, respectively. The errors between the GLMF and RVEF are presented in Fig. 11, and the errors is caused by round-off error.
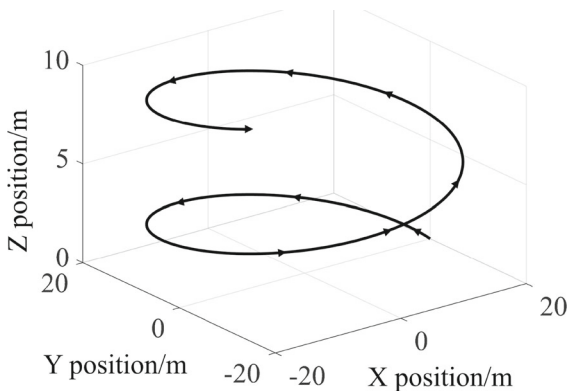
Simulation results indicate that the GLMF achieves the same accuracy as the RVEF and Euler frames.

The parameters of Case 1 are presented in Table 1, demonstrating that the GLMF is more efficient than the RVEF and Euler frames. Since the dynamic equations in the GLMF are all established in global frame, there is no need for transformations between the global frame and the element frame. Consequently, the calculations of the mass matrix and force vectors require less time compared to the Euler and RVEF frames.

2.6 Singularity of element frames

The singularities of the Euler, Frenet, RVEF and GLMF frames are introduced in this section. Due to the characteristic of arctangent function, the Euler frame is singular when the value of $\theta_{ele\,i}$ and $\varphi_{ele\,i}$ are within special ranges. These singular ranges are shown in Fig. 12. The transformation matrix $\mathbf{A}_{ele\,i}^{trans}$ is invalid within these ranges.

The Frenet frame is singular when some cable nodes form a straight line, making it impossible to determine the normal vector. The two terminal nodes and the virtual node are collinear in these situations. According to Eq. (14), the normal vector $\mathbf{n}_{ele\,i}'$ becomes a zero vector, rendering the normal vector meaningless. The $\mathbf{A}_{ele\,i}^{trans}$ is also invalid.

For the RVEF, singularities occur when the relative velocity $\mathbf{v}_{ele\,i}^{g}$ is parallel with the tangential vector $\mathbf{z}_{ele\,i}^{g}$. In such case, both the normal and binormal vectors become meaningless, rendering the transformation matrix invalid.
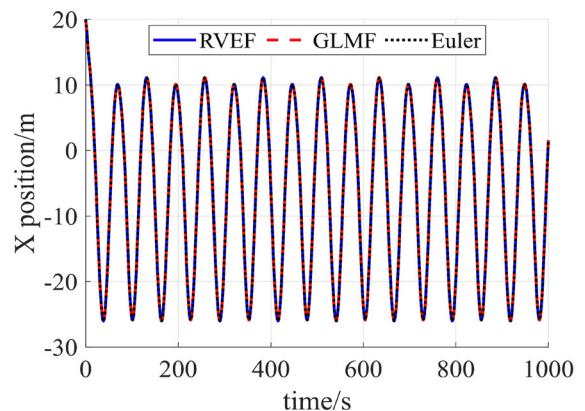

Fig. 6 Initial positions of cable

Fig. 7 Trace of the top node

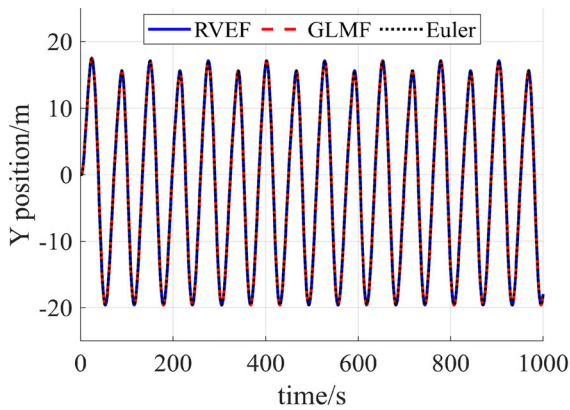Fig. 8 X-position of last node
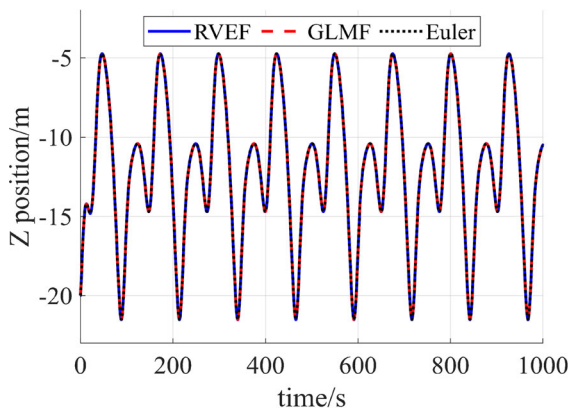
Fig. 9 Y-position of last node

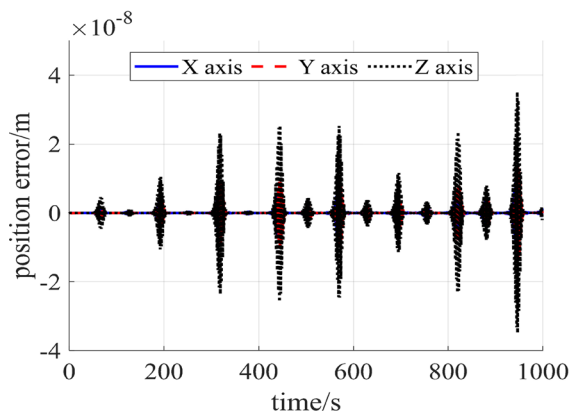**Fig. 10** Z-position of last node

Fig. 11 Position errors between GLMF and RVEF

The GLMF may be singular when the element length is zero. However, this situation is impossible in cable dynamics, ensuring that the GLMF has no singularities. The singularities of the four frames mentioned above are summarized in Table 2.

3 Cable model by ALE-GLMF

3.1 ALE-GLMF

The ALE-GLMF, combining the ALE and GLMF, is proposed to model underwater cables with variable lengths. To account for the changing length of the cable, a physical coordinate p is added to each cable element, as shown in Fig. 13.

The coordinates of element i $\mathbf{q}_{ele\,i}$ are written as,

$$\mathbf{q}_{ele\,i} = \begin{bmatrix} \mathbf{r}_{node\,i}^T & \mathbf{r}_{node\,i+1}^T & p_{node\,i} & p_{node\,i+1} \end{bmatrix}^T \quad (32)$$

A variable s is needed to express the node position in element i.

$$s = \frac{2p - p_{node\,i} - p_{node\,i+1}}{p_{node\,i} - p_{node\,i+1}} \quad (33)$$

The position vector of the arbitrary node in element i is written as,

$$\begin{cases} \mathbf{q}_{ele\,i}^e = \begin{bmatrix} \mathbf{r}_{node\,i}^T & \mathbf{r}_{node\,i+1}^T \end{bmatrix}^T \\ \mathbf{N}_e = \begin{bmatrix} \dfrac{1-s}{2}\mathbf{I}_{3\times3} & \dfrac{1+s}{2}\mathbf{I}_{3\times3} \end{bmatrix} \\ \mathbf{r} = \mathbf{N}_e\mathbf{q}_{ele\,i}^e \end{cases} \quad (34)$$

where $\mathbf{r}$ is the node position vector with respect to the global frame.

The velocity vector of the arbitrary node in element i is written as,

$$\begin{cases} \mathbf{N} = \begin{bmatrix} \mathbf{N}_e & \dfrac{\partial \mathbf{N}_e}{\partial p_{node\,i}}\mathbf{q}_{ele\,i}^e & \dfrac{\partial \mathbf{N}_e}{\partial p_{node\,i+1}}\mathbf{q}_{ele\,i}^e \end{bmatrix} \\ \dot{\mathbf{r}} = \mathbf{N}\dot{\mathbf{q}}_{ele\,i} \end{cases} \quad (35)$$

where $\dot{\mathbf{r}}$ is the node velocity with respect to the global frame.

The acceleration vector of the arbitrary node in element i is written as Eq. (36),

Table 1 Parameters of case 1

Parameters value	d_c (m)	C_{dt}	C_{dn}	C_m		E (N/m²)	ρ_c (kg/m³)
	0.04	0.01	1.15	0.2		5×10^{10}	4000
Parameters value	ρ_f (kg/m³)	c	n_{node}	$\mathbf{v}_w$ (m/s)	$\mathbf{a}_w$ (m/s²)	Simulation time (s)	
	1025	10^{-5}	11	$[-1\ 0\ 0]^T$	$[0\ 0\ 0]^T$	1000	
Parameters value	Computation time of RVEF (s)				Computation time of GLMF (s)		
	179.87				156.82		
Parameters value	Computation time of Euler (s)						
	182.81						
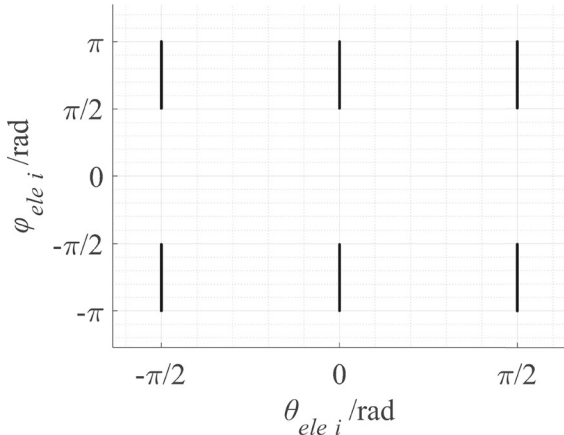
Fig. 12 Singularity ranges of Euler frame

$$\begin{cases} \ddot{\mathbf{r}}_p = 2\left(\dfrac{\partial \mathbf{N}_e}{\partial p_{node\,i}}\dot{p}_{node\,i} + \dfrac{\partial \mathbf{N}_e}{\partial p_{node\,i+1}}\dot{p}_{node\,i+1}\right)\dot{\mathbf{q}}_e + \\[2mm] \left(\begin{aligned} &\dfrac{\partial^2 \mathbf{N}_e}{\partial p_{node\,i}^2}\dot{p}_{node\,i}^2 + 2\dfrac{\partial^2 \mathbf{N}_e}{\partial p_{node\,i}\partial p_{node\,i+1}}\dot{p}_{node\,i}\dot{p}_{node\,i+1} \\ &\hspace{2cm} + \dfrac{\partial^2 \mathbf{N}_e}{\partial p_{node\,i+1}^2}\dot{p}_{node\,i+1}^2 \end{aligned}\right)\mathbf{q}_e \\[2mm] \ddot{\mathbf{r}} = \mathbf{N}\ddot{\mathbf{q}}_{ele\,i} + \ddot{\mathbf{r}}_p \end{cases}$$
$$(36)$$

where $\ddot{\mathbf{r}}$ is the node acceleration with respect to the global frame.

The axial strain of an arbitrary node in element i is written as Eq. (37) [34–36],

$$\begin{cases} \dfrac{d\mathbf{r}}{dp} = \dfrac{\partial \mathbf{N}_e}{\partial p}\mathbf{q}_{ele\,i}^e \\[2mm] \varepsilon_0 = \dfrac{1}{2}\left[\left(\dfrac{d\mathbf{r}}{dp}\right)^T\dfrac{d\mathbf{r}}{dp} - 1\right] \end{cases}$$
$$(37)$$

where ε_0 is the axial strain.

According to the element forces, the forces acting on the nodes i and $i+1$ can be divided into three parts, as shown in Eq. (38).

$$\begin{bmatrix} \mathbf{F}_{node\,i} \\ \mathbf{F}_{node\,i+1} \end{bmatrix} = \begin{bmatrix} \mathbf{F}_{node\,i}^p \\ \mathbf{F}_{node\,i+1}^p \end{bmatrix} + \begin{bmatrix} \mathbf{F}_{node\,i}^e \\ \mathbf{F}_{node\,i+1}^e \end{bmatrix} + \begin{bmatrix} \mathbf{F}_{node\,i}^{ex} \\ \mathbf{F}_{node\,i+1}^{ex} \end{bmatrix}$$
$$(38)$$

where $\mathbf{F}_{node\,i}^{in}$ and $\mathbf{F}_{node\,i}^{ex}$ are the internal force and external forces of the node i, respectively. $\mathbf{F}_{node\,i}^p$ is the force induced by the physical velocity of the nodes i and $i+1$. $\mathbf{F}_{node\,i}^p$ is zero and the ALE-GLMF simplifies to the GLMF when the cable length is constant. In other words, ALE-ANCF can model the variable-length cable due to the inclusion of $\mathbf{F}_{node\,i}^p$.

The mass flow forces $\mathbf{F}_{node\,i}^p$ and $\mathbf{F}_{node\,i+1}^p$ are expressed as,

$$\begin{bmatrix} \mathbf{F}_{node\,i}^p \\ \mathbf{F}_{node\,i+1}^p \end{bmatrix} = -\frac{p_{node\,i+1} - p_{node\,i}}{2}\int_{-1}^{1}\rho_f A\mathbf{N}^T\ddot{\mathbf{r}}_p ds$$
$$(39)$$

The internal forces $\mathbf{F}_{node\,i}^{in}$ and $\mathbf{F}_{node\,i+1}^{in}$ acting on the element i are shown in Eq. (40), which can be found in references [37, 38],

Table 2 Singularity range of four frames

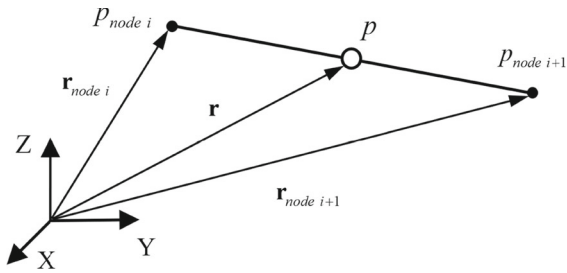| Frame	Singularity case
Euler frame	Figure 12
Frenet frame	Cable shape function is a straight line
RVEF	Relative velocity and tangential direction are parallel
GLMF	No singularity

Fig. 13 Position vector of arbitrary node within element

$$\begin{bmatrix} \mathbf{F}^{in}_{node\,i} \\ \mathbf{F}^{in}_{node\,i+1} \end{bmatrix} = - \frac{p_{node\,i+1} - p_{node\,i}}{2}$$
$$\times \int_{-1}^{1} \left[\left(\frac{\partial \varepsilon_0}{\partial \mathbf{q}_{ele\,i}} \right)^T EA(\varepsilon_0 + c\dot{\varepsilon}_0) \right] ds \tag{40}$$

The external forces $\mathbf{F}^{ex}_{node\,i}$ and $\mathbf{F}^{ex}_{node\,i+1}$ are shown in Eq. (41),

$$\begin{bmatrix} \mathbf{F}^{ex}_{node\,i} \\ \mathbf{F}^{ex}_{node\,i+1} \end{bmatrix} = \frac{p_{node\,i+1} - p_{node\,i}}{2} \int_{-1}^{1} \mathbf{N}^T \mathbf{f} ds \tag{41}$$

where $\mathbf{f}$ is the external force acting on the infinitesimal body as shown in Eq. (42) [39, 40].

$$\begin{cases} \mathbf{t} = \dfrac{d\mathbf{r}/dp}{\|d\mathbf{r}/dp\|} \\ \mathbf{P} = \mathbf{I}_{3\times3} - \mathbf{t}\mathbf{t}^T \\ \mathbf{f} = \dfrac{1}{2} C_n \rho_f d_c \|\mathbf{P}\mathbf{v}\| \mathbf{P}\mathbf{v} + \\ \dfrac{\pi}{2} C_f \rho_f d_c |\mathbf{t}^T \mathbf{v}| \mathbf{t}\mathbf{t}^T \mathbf{v} + (1 + C_m) A \rho_f \mathbf{P}\mathbf{a}_w \end{cases} \tag{42}$$

The mass matrices of nodes i and $i + 1$ are written as,

$$\begin{bmatrix} \mathbf{M}_{node\,i} & \mathbf{0} \\ \mathbf{0} & \mathbf{M}_{node\,i+1} \end{bmatrix} = \frac{p_{node\,i+1} - p_{node\,i}}{2}$$
$$\times \int_{-1}^{1} \mathbf{N}^T (\rho_c A \mathbf{I}_{3\times3} + \mathbf{M}_{add}) \mathbf{N} ds \tag{43}$$

The additional mass matrix of element i is written as,

$$\mathbf{M}_{add} = C_m \rho_f A \mathbf{P} \tag{44}$$

The ALE-GLMF introduces additional constraint equations derived from ALE. These constraint equations are related to the physical coordinates of all nodes and are expressed as,

$$p_{node\,i} - f(t, \mathbf{q}, \dot{\mathbf{q}}) = 0 \tag{45}$$

where f is a function used to calculate these constraints.

3.2 Simulation results

The ALE-ANCF is a finite method to establish the dynamic model of a beam with a variable length. It expresses the dynamic equations using the position, gradient and physical coordinates of the element terminal nodes, as shown in Eq. (46) [17].

$$\mathbf{q}_{ele\,i} = \begin{bmatrix} \mathbf{r}^T_{node\,i} & \mathbf{r}'^T_{node\,i} & p_{node\,i} \\ \mathbf{r}^T_{node\,i+1} & \mathbf{r}'^T_{node\,i+1} & p_{node\,i+1} \end{bmatrix}^T \tag{46}$$

where $\mathbf{r}'^T_{node\,i}$ and $\mathbf{r}'^T_{node\,i+1}$ are gradient coordinates of nodes i and $i + 1$, respectively.

The gradient coordinates are included in ALE-ANCF, allowing for a more precise expression of bending effects compared to ALE-GLMF. The internal forces, including the bending force, are shown in Eq. (47).

$$\begin{cases} \kappa = \dfrac{\|d^2\mathbf{r}/dp^2 \times d\mathbf{r}/dp\|}{\|d\mathbf{r}/dp\|^3} \\ \begin{bmatrix} \mathbf{F}^{in}_{node\,i} \\ \mathbf{F}^{in}_{node\,i+1} \end{bmatrix} = - \dfrac{p_{node\,i+1} - p_{node\,i}}{2} \int_{-1}^{1} \left[\left(\dfrac{\partial \varepsilon_0}{\partial \mathbf{q}_{ele\,i}} \right)^T EA(\varepsilon_0 + c\dot{\varepsilon}_0) + \left(\dfrac{\partial \kappa}{\partial \mathbf{q}_{ele\,i}} \right)^T EJ(\kappa + c\dot{\kappa}) \right] ds \end{cases} \tag{47}$$

where κ is the curvature of the node corresponding to the physical coordinate p. J represents the cross-sectional moment of inertia.

To compare the accuracy of ALE-GLMF with that of ALE-ANCF in modeling cable deployments, circle, straight-line, and screw routes are simulated in Case 2. To enhance the accuracy of ALE-GLMF, the element length is set to 5 m, compared to 50 m for ALE-ANCF. The number of elements varies with the cable length. According to the previous work by Hong [18], the generation and elimination of nodes follow specific rules (Fig. 14):

(1) A new node is inserted when the length-variable element becomes 1.5 times longer than the standard length.
(2) An old node is deleted when the length-variable element becomes 0.5 times shorter than the standard length.

The initial positions of Case 2 are depicted in Fig. 15, with a 1000 kg mass point placed at the end of the cable. The modeling parameters are summarized in Table 3. The variation in cable length over time is illustrated in Fig. 16.

The traces of the top node in the circle, straight-line, and screw routes are shown in Fig. 17, respectively. The diameter of the screw route is 40 m, with the top node traveling 62.8 m along the Z-axis for every circular motion completed in 62.8 s. Only the first 100 s of the screw route is depicted here. The X-, Y-, and Z-coordinates of the last node over time for these routes are shown in Figs. 18, 19, 20. Since the cable motion in the straight-line route exists only in the XZ plane, the Y-position is omitted herein. The three-dimensional cable shapes using ALE-GLMF and ALE-ANCF at the 2000th second are presented in Fig. 21. The cable positions calculated using ALE-

GLMF are so close to those using ALE-ANCF that it is difficult to distinguish the position differences in Figs. 18, 19, 20, 21.

Therefore, the position differences for Case 2 are illustrated in Fig. 22. The relative errors represent the absolute position differences divided by the unstretched cable length over time. The maximum relative position error is around the 10^{-4} level, indicating that the ALE-GLMF achieves nearly the same accuracy as ALE-ANCF in these scenarios.

These scenarios demonstrate that the ALE-GLMF performs well in modeling marine towing systems under both straight towing and circular turning conditions. Due to the minimal bending flexural modulus in ropes or cables, the ALE-GLMF with a shorter element length can achieve nearly identical accuracy to ALE-ANCF with a longer element length. Moreover, the ALE-GLMF formula is much easier to understand and code compared to the ALE-ANCF formula.

The computational time for Case 2 is shown in Table 4. Since bending deformation can be accurately expressed by ANCF with a larger element length compared to GLMF, the number of nodes in the cable modeled by ALE-ANCF is 1/10 of that in the ALE-GLMF model. Consequently, the computational time for ALE-ANCF is about 1/3 of that for ALE-GLMF in circular and screw routes. However, the advantage of ALE-ANCF is reduced in the straight route. Therefore, ALE-GLMF is suitable for situations where the bending deformation is negligible.
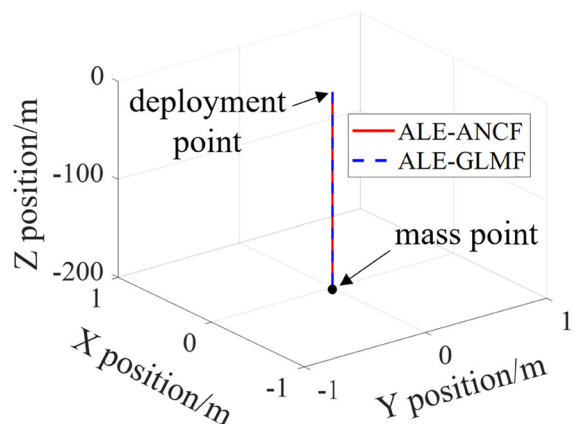

Fig. 14 Illustration of node insertion and deletition

Fig. 15 Initial positions of cable

Table 3 Parameters of case 2

Parameters value	d_c (m)	C_{dt}	C_{dn}	C_m	E (N/m^2)	ρ_c (kg/m^3)
	0.04	0.01	2	0.2	5e10	4000
Parameters value	ρ_f (kg/m^3)	c	$\mathbf{v}_w$ (m/s)	$\mathbf{a}_w$ (m/s^2)	Simulation time (s)	
	1025	10^{-5}	$[1\ 0\ 0]^T$	$[0\ 0\ 0]^T$	2000	
Parameters value	Element length in ALE-ANCF (m)				Element length in ALE-GLMF (m)	
	50				5	
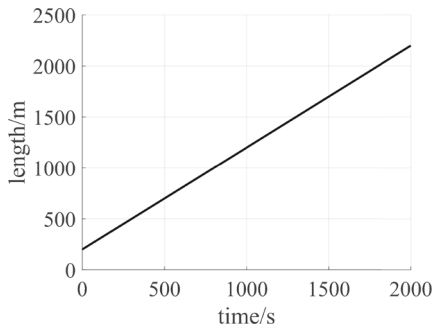
Fig. 16 cable length variation over time

Case 3 demonstrates the performance of ALE-GLMF when the cable comes into contact with the seabed. The contact force is expressed as,

$$\begin{cases} \mathbf{F}^N_{node\ i} = Kl_{ele\ i}(z_{seabed} - z_{node\ i})[0\ \ 0\ \ 1]^T \\ \mathbf{F}^d_{node\ i} = -Cl_{ele\ i}\dot{z}_{node\ i}[0\ \ 0\ \ 1]^T \\ \mathbf{F}^f_{node\ i} = -\mu\|\mathbf{F}^N_{node\ i}\|\dfrac{\dot{\mathbf{r}}_{node\ i}}{\|\dot{\mathbf{r}}_{node\ i}\|} \end{cases} \quad (48)$$

where $\mathbf{F}^N_{node\ i}$, $\mathbf{F}^d_{node\ i}$ and $\mathbf{F}^f_{node\ i}$ are the support force, damping force and friction force at node i, respectively. K and C are the stiffness and damping
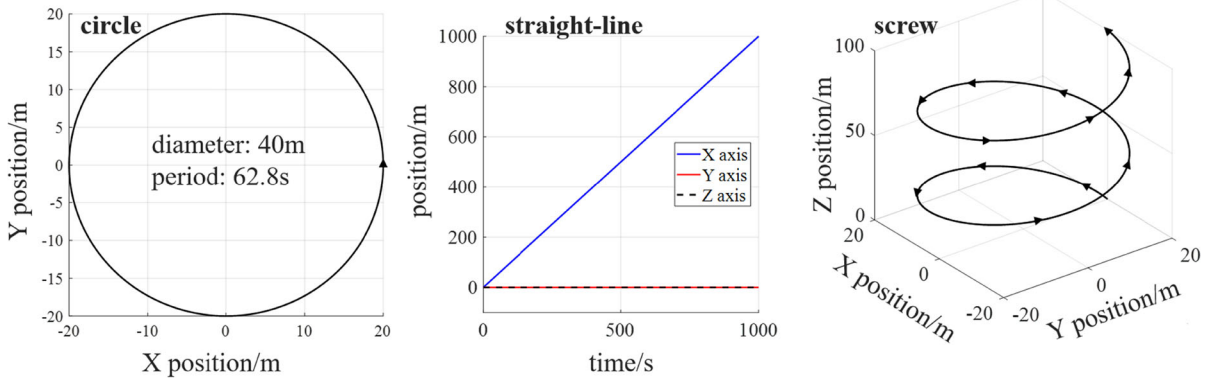
Fig. 17 Trace of top node in circle, straight-line and screw routes
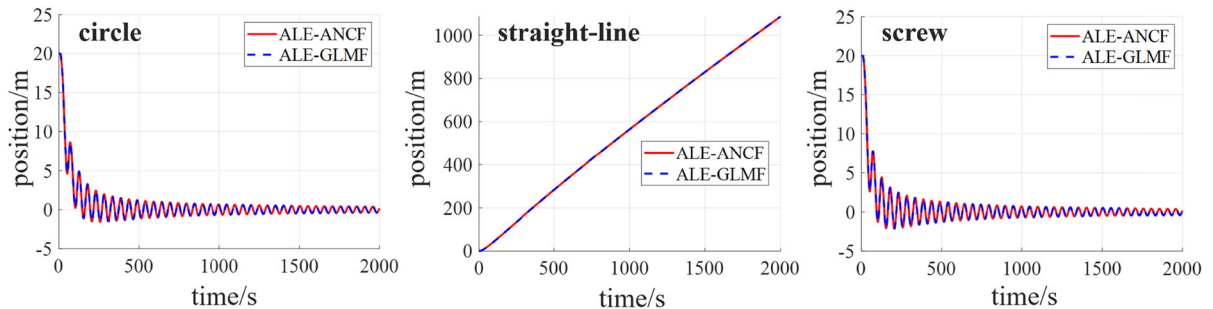
Fig. 18 X-position of last node

Fig. 19 Y-position of last node
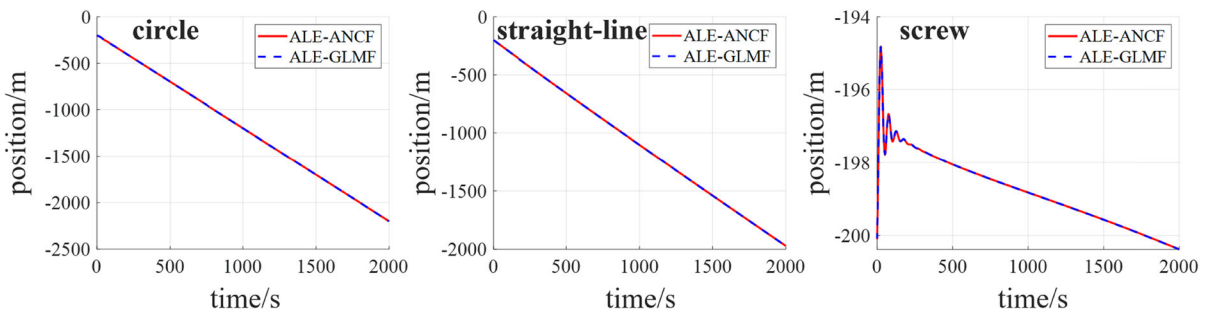
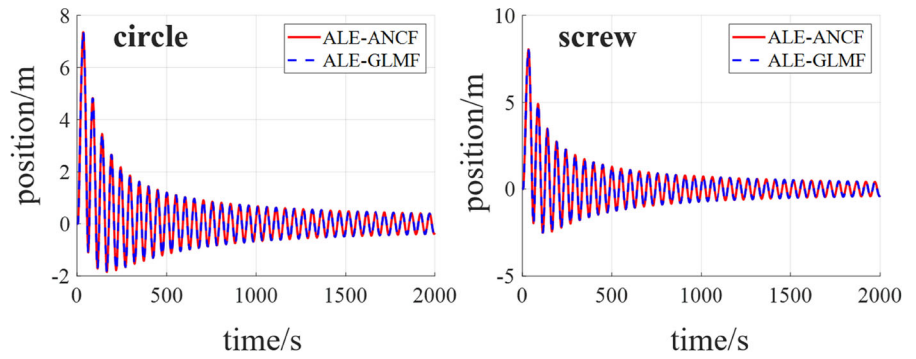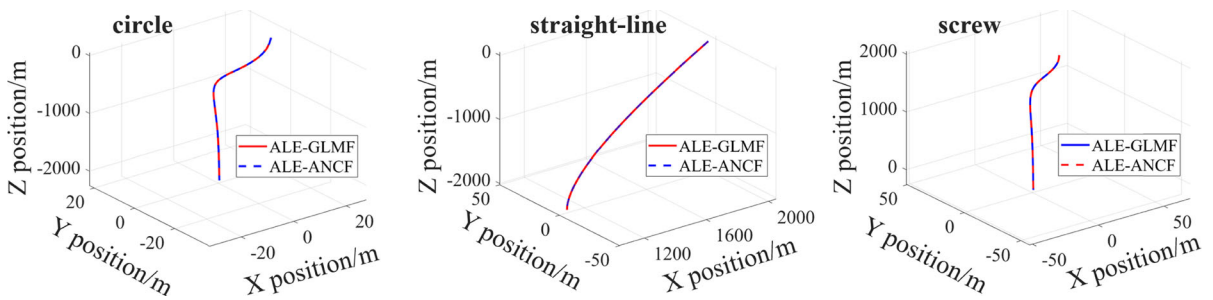

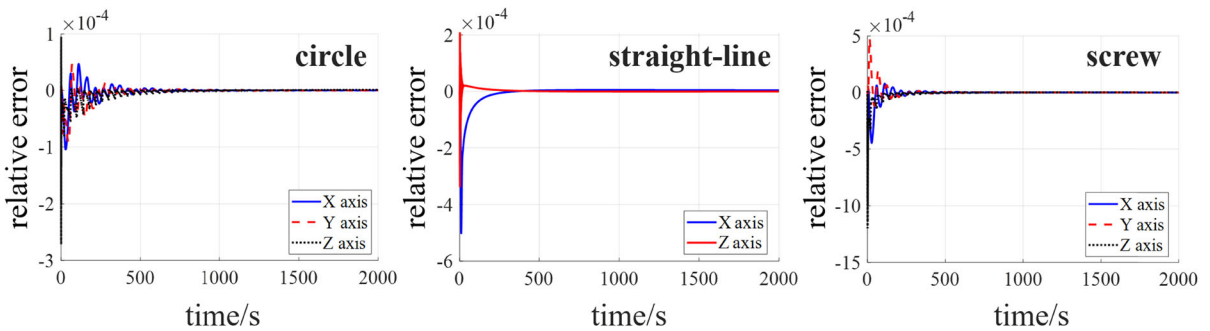Fig. 20 Z-position of last node

Fig. 21 Cable shape at 2000th

Fig. 22 Position error of last node

coefficients of the normal contact, respectively. μ represents the friction coefficient of contact. z_{seabed} is the z coordinate of seabed. $z_{node\ i}$ and $\dot{z}_{node\ i}$ represent the z-directional position and velocity of node i.

The contact force between cable and seabed of ALE-ANCF element is written as,

$$\mathbf{f}_{contact} = K(z_{seabed} - z_{\mathbf{r}})[0 \quad 0 \quad 1]^T$$
$$- Cl_{ele\ i}\dot{z}_{\mathbf{r}}[0 \quad 0 \quad 1]^T - \mu K|z_{seabed} - z_{\mathbf{r}}|\frac{\dot{\mathbf{r}}}{\|\dot{\mathbf{r}}\|}$$
(49)

where $\mathbf{f}_{contact}$ is the contact force, $z_{\mathbf{r}}$ is the z-coordinate of vector $\mathbf{r}$, and $\dot{z}_{\mathbf{r}}$ is the velocity in Z-axis. The external force of ALE-ANCF is written as,

$$\begin{cases} \mathbf{f} = \dfrac{1}{2}C_n\rho_f d_c\|\mathbf{Pv}\|\mathbf{Pv} + \dfrac{\pi}{2}C_f\rho_f d_c|\mathbf{t}^T\mathbf{v}|\mathbf{tt}^T\mathbf{v} \\ \qquad + (1+C_m)A\rho_f\mathbf{Pa}_w + \mathbf{f}_{contact} \\ \begin{bmatrix} \mathbf{F}_{node\ i}^{ex} \\ \mathbf{F}_{node\ i+1}^{ex} \end{bmatrix} = \dfrac{p_{node\ i+1} - p_{node\ i}}{2}\displaystyle\int_{-1}^{1}\mathbf{N}^T\mathbf{f}ds \end{cases}$$
(50)

The initial shape of cable is shown in Fig. 23, and the top node of cable is driven by a straight-line route, as shown in Fig. 24. The variation of the cable length over time is illustrated in Fig. 25. The simulation result of ALE-ANCF and ALE-GLMF are presented in Figs. 26, 27, 28.

Table 4 Computational time for case 2

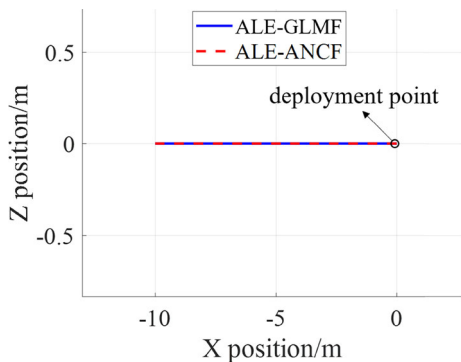| Route type	ALE-ANCF	ALE-GLMF
Circle	1816.66 s	5287.78 s
Straight	1200.45 s	1999.09 s
Screw	1737.97 s	4972.51 s

Fig. 23 Initial positions

Simulation results indicate that the cable modeled by ALE-GLMF exhibits broken lines when the elements start to contact with the seabed, as illustrated
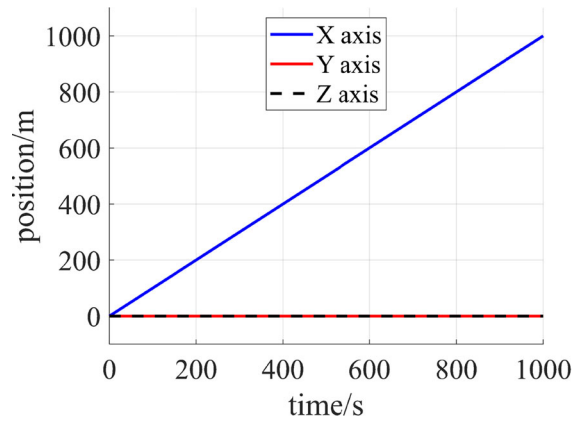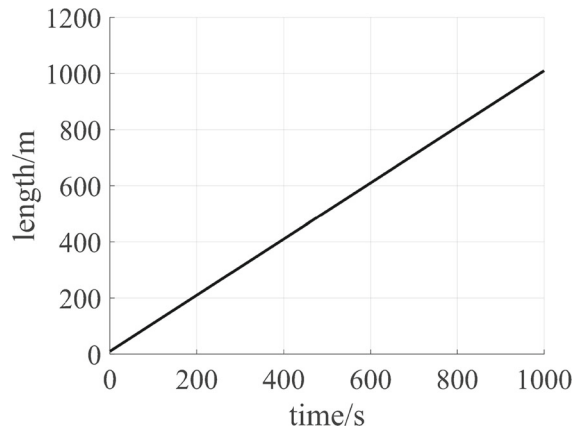

Fig. 24 Trace of the top node

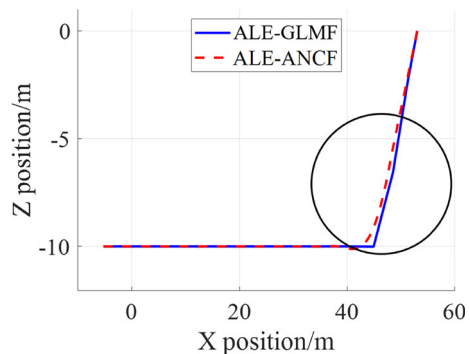**Fig. 25** cable length variation over time

Fig. 26 Cable shape at the 53th s

by black circles in Figs. 26, 27, 28. While, the cable modeled by ALE-ANCF consistently presents smooth, continuous curves. Based on lump mass method, the cable element in ALE-GLMF only has axial deformation and cannot express bending deformation within element, whereas, the bending deformation is well expressed by the element of ALE-ANCF.
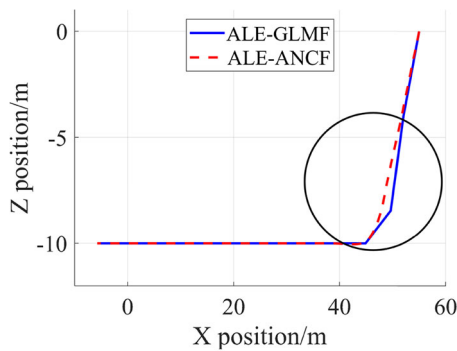

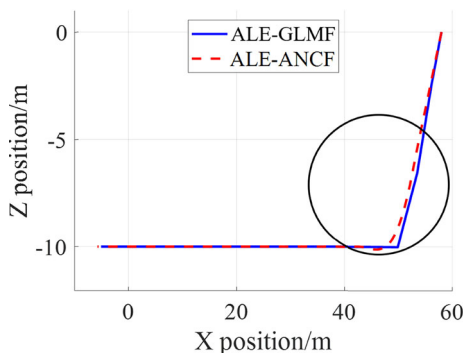**Fig. 27** Cable shape at the 56th s

Fig. 28 Cable shape at the 58th s

Although the accuracy of ALE-GLMF is lower than that of ALE-ANCF in expressing bending deformation, the cable elements that have contacted with seabed show almost the same accuracy as ALE-ANCF. Additionally, the computational time of ALE-GLMF is much less than that of ALE-ANCF, as shown in Table 5. Therefore, ALE-GLMF has advantages in analyzing the cases where the bending deformation within elements is negligible, and many cable nodes are needed to express contact or concentrated mass points.

4 Conclusion

This paper addresses the singularity issues associated with traditional lumped mass methods in modeling underwater cables by proposing a Global Lumped Mass Formulation (GLMF) expressed solely using global nodal coordinates. Additionally, the combination of Arbitrary Lagrangian–Eulerian (ALE) and GLMF results in the ALE-GLMF, suitable for modeling cables with variable lengths, commonly used in marine towing and cable laying systems. The performance of ALE-GLMF is validated against ALE-ANCF, which employs third-order shape functions to express cable deformation. The key conclusions are as follows:

(1) GLMF avoids singularity issues in transformation matrices by directly expressing all element forces and masses using global node coordinates, distinguishing it from the Euler frame, Frenet frame, and RVEF.

(2) GLMF outperforms traditional element frames in efficiency due to the absence of an element frame.

Table 5 Parameters of case 3

Parameters value	d_c (m)	C_{dt}	C_{dn}	C_m	E (N/m^2)
	0.04	0. 01	1	1	7.02×10^7
Parameters value	ρ_c (kg/m^3)	$l_{ele\ i}$ (m)	K (N/m^2)	μ	ρ_f (kg/m^3)
	4000	5	400	0.01	1025
Parameters value	c	$\mathbf{v}_w$ (m/s)	$\mathbf{a}_w$ (m/s^2)	z_{seabed} (m)	C(N·s/m^2)
	10^{-5}	$[0\ 0\ 0]^T$	$[0\ 0\ 0]^T$	-10	100
Parameters Value	Simulation time(s)	Computation time of ALE-ANCF		Computation time of ALE-GLMF	
	1000	20,070.05 s		5054.68 s	

(3) Because each GLMF node requires only 3 coordinates compared to the 6 coordinates of ANCF nodes, GLMF offers greater computational efficiency than ANCF when they have the same number of nodes.

(4) GLMF requires much shorter element lengths to achieve the same accurate as ANCF in expressing cable bending behaviors, which spends more computational time than ANCF.

(5) ALE-GLMF effectively models cable deployment and retrieval in marine towing and cable laying systems.

(6) GLMF and ALE-GLMF are preferable for cables with low bending deformation, particularly in scenarios requiring numerous cable nodes to express concentrated loads or mass points.

(7) Overall, GLMF and ALE-GLMF offer robust solutions for modeling underwater cables, particularly in scenarios with low bending deformation and complex loading conditions.

Data availability Enquiries about data availability should be directed to the authors.

Declarations

Conflict of interest The authors declare that they have no known competing financial interests or personal relationships that could have appeared to influence the work reported in this paper.

References

1. Zhu, X.Q., Wei, Z.R., Pei, Y.L., Yu, K.B., Zong, L.: Dynamic modeling and position prediction of deep-towed seismic array. J. Shandong Univ. Eng. Sci. **50**(6), 9–16 (2020)

2. Zhu, X.Q., Bi, Q.X., Li, X.Y., Ryan, N.O., Li, G.Q., Ren, H.: Effect of bottom counterweight and cable distribution on the hydrodynamic response of the gravity net cage. Ships Offshore Struct. **18**(1), 120–129 (2023)

3. Zhu, X.Q., Li, X.Y., Pei, Y.L., Ren, H., Choi, J.H.: An efficient surrogate model-based method for deep-towed seismic system optimization. Ocean Eng. **268**, 113463 (2023)

4. Shen, H.B., Zhao, Y.P., Bi, C.W., Xu, Z.J.: Nonlinear dynamics of an aquaculture cage array induced by wave-structure interactions. Ocean Eng. **269**, 113711 (2023)

5. Feng, H., Sun, W.B., Tang, G.Y., Wang, J.J.: Study on a novel two-part underwater towed system for near-surface towed vehicle test. Ocean Eng. **255**, 111440 (2022)

6. Xin, S.Z., Wang, Y.T., Wang, L., Wang, X.F.: A safety assessment approach of the salvage based on salvor–cable–wreck coupled simulations. Ocean Eng. **269**, 113537 (2023)

7. Zhang, D.P., Zhao, B.W., Zhu, K.Q., Jiang, H.Y.: Dynamic response of deep-sea trawl system during towing process. J. Mar. Sci. Eng. **11**(1), 145 (2023)

8. Chen, X.H., Liu, B., Le, G.G.: Numerical simulation research on the anchor last deployment of marine submersible buoy system based on VOF method. J. Mar. Sci. Eng. **10**(11), 1681 (2022)

9. Pan, Y., Yang, F.T., Tong, H.H., Zuo, X., Shen, L.D., Xue, D.W., Liu, C.: Experimental and numerical simulation of a symmetrical three-cylinder Buoy. Symmetry-Basel **14**(5), 1057 (2022)

10. Wang, N.G., Xiang, X.Q., Jiang, Y.Y., Yang, R.G.: Modelling and vibration control for deep-sea robot lifting system with time variable length and nonlinear disturbance observer. Ocean Eng. **246**, 110558 (2022)

11. Hong, S.M., Ha, K.N., Kim, J.Y.: Dynamics modeling and motion simulation of USV/UUV with linked underwater cable. J. Mar. Sci. Eng. **8**(5), 318 (2020)

12. Du, X.X., Cui, H., Zhang, Z.D.: A numerical method for analyzing the influence of underwater vehicle flow field on dynamic behavior of towed sonar cable array. Ocean Eng. **175**, 163–175 (2019)

13. Zheng, Z.Q., Xu, J.P., Huang, P., Wang, L., Yang, X.G., Chang, Z.Y.: Dynamics of anchor last deployment of submersible buoy system. J. Ocean Univ. China **15**(1), 69–77 (2016)

14. Ranganathan, S.I.: A novel finite element model incorporating rotary inertia in thin circular rods. Proceed Inst. Mech. Eng. Part C-J. Mech. Eng. Sci. **227**(10), 2386–2390 (2013)

15. Bertrand, C., Savadkoohi, A.T., Acary, V., Lamarque, C.H.: Reduced-order model for the nonlinear dynamics of cables. J. Eng. Mech. **148**(9), 04022052 (2022)

16. Zhu, X.Q., Yoo, W.S.: Suggested new element reference frame for dynamic analysis of marine cables. Nonlinear Dyn. **87**(1), 489–501 (2017)

17. Liu, D.P., Ai, S.M., Sun, L.P.: ALE-ANCF modeling of the lowering process of a J-lay pipeline coupled with dynamic positioning. Ocean Eng. **269**, 113552 (2023)

18. Hong, D.F., Ren, G.X.: A modeling of sliding joint on one-dimensional flexible medium. Multibody Sys.Dyn. **26**(1), 91–106 (2011)

19. Polachek, H., Walton, T.S., Mejia, R., Dawson, C.D.: Transient motion of an elastic cable immersed in a fluid. Math. Comput. **17**, 60–63 (1963)

20. Walton, T.S., Polachek, H.: Calculation of transient motion of submerged cables. Math. Comput. **14**, 27–46 (1960)

21. Zhu, X.Q., Wang, Y.F., Yoo, W.S., Nicoll, R., Ren, H.: Stability analysis of spar platform with four mooring cables in consideration of cable dynamics. Ocean Eng. **236**, 109522 (2021)

22. Baumgarte, J.: Stabilization of constraints and integrals of motion in dynamical systems. Comput. Methods Appl. Mech. Eng. **1**(1), 1–16 (1972)

23. Adamiec, W.I., Brzozowska, L., Wojciech, S.: Effectiveness of the segment method in absolute and joint coordinates when modelling risers. Acta Mech. **231**(2), 435–469 (2020)

24. Diebel, J.: Representing attitude: Euler angles, unit quaternions, and rotation vectors. Matrix Stuttg. Ger. **58**(15–16), 1–35 (2006)

25. Bauer, J.D.: Calculus: Early transcendentals. WH Freeman, New York (2015)

26. Palm, J., Eskilsson, C.: Mooring systems with submerged buoys: influence of buoy geometry and modelling fidelity. Appl. Ocean Res. **102**, 102302 (2020)

27. Petrone, C., Oliveto, N.D., Sivaselvan, M.V.: Dynamic analysis of mooring cables with application to floating offshore wind turbines. J. Eng. Mech. **142**(3), 04015101 (2016)

28. Jin, C.K., Kim, G.J., Kim, S.J., Kim, M., Kwak, H.G.: Discrete-module-beam-based hydro-elasticity simulations for moored submerged floating tunnel under regular and random wave excitations. Eng. Struct. **275**, 115198 (2023)

29. Pegalajar, J., Bredmose, H.: Reproduction of slow-drift motions of a floating wind turbine using second-order hydrodynamics and operational modal analysis. Mar. Struct. **66**, 178–196 (2019)

30. ProteusDS: ProteusDS Manual. Canada (2018)

31. Han, C.Y., Kwon, S.H.: Cubic helical splines with Frenet-frame continuity. Comput. Aided Geom. Des. **28**(7), 395–406 (2011)

32. David, C.L.: Linear algebra and its applications. Cengage Learning, Singapore (2004)

33. Roger, A., Charles, R.: Matrix analysis. Cambridge University Press, United Kingdom (2012)

34. Yang, S.M., Zhu, X.Q., Ren, H.: Dynamic analysis of a deep-towed seismic system based on a flexible multi-body dynamics frame. Ocean Eng. **279**, 114587 (2023)

35. Shabana, A.A.: Definition of the slopes and the finite element absolute nodal coordinate formulation. Multibody Syst. Dyn. **1**(3), 339–348 (1997)

36. Shabana, A.A.: Definition of ANCF finite elements. J. Comput. Nonlinear Dyn. **10**(5), 054506 (2015)

37. Fan, W., Ren, H., Zhu, W.D., Zhu, H.: Dynamic analysis of power transmission lines with ice-shedding using an efficient absolute nodal coordinate beam formulation. J. Comput. Nonlinear Dyn. **16**(1), 011005 (2021)

38. Ren, H.: A simple absolute nodal coordinate formulation for thin beams with large deformations and large rotations. J. Comput. Nonlinear Dyn. **10**(6), 061005 (2015)

39. Liu, D.P., Ai, S.M., Sun, L.P., Wei, J.Y., He, N.: Numerical modelling of offshore risers conveying slug flow under the ALE–ANCF framework. Ocean Eng. **235**, 109415 (2021)

40. Zhang, C., Lu, L., Cao, Q.Y., Cheng, L., Tang, G.Q.: Nonlinear motion regimes and phase dynamics of a free standing hybrid riser system subjected to ocean current and vessel motion. Ocean Eng. **252**, 111197 (2022)